

A new noninvasive and patient-specific hemodynamic index for the severity of renal stenosis and outcome of interventional treatment

Huidan Yu^{1,2} | Monsurul Khan¹ | Hao Wu¹ | Xiaoping Du¹ | Rou Chen¹ |
 Dave M. Rollins³ | Xin Fang⁴ | Jianyun Long⁴ | Chenke Xu⁵ |
 Alan P. Sawchuk²

¹Department of Mechanical and Energy Engineering, Indiana University-Purdue University, Indianapolis (IUPUI), Indianapolis, Indiana, USA

²Department of Surgery, Indiana University School of Medicine, Indianapolis, Indiana, USA

³Vascular Diagnostic Center, Indiana University Health, Indianapolis, Indiana, USA

⁴Department of Vascular Surgery, The Affiliated Hangzhou First People's Hospital, Zhejiang University School of Medicine, Hangzhou, China

⁵Department of Ultrasound, The Affiliated Hangzhou First People's Hospital, Zhejiang University School of Medicine, Hangzhou, China

Correspondence

Huidan Yu, Department of Mechanical and Energy Engineering, Indiana University-Purdue University, Indianapolis (IUPUI), IN 46278, USA.
 Email: whyu@iupui.edu

Present address

Monsurul Khan, School of Mechanical Engineering, Purdue University, West Lafayette, Indiana, USA

Abstract

Renal arterial stenosis (RAS) often causes renovascular hypertension, which may result in kidney failure and life-threatening consequences. Direct assessment of the hemodynamic severity of RAS has yet to be addressed. In this work, we present a computational concept to derive a new, noninvasive, and patient-specific index to assess the hemodynamic severity of RAS and predict the potential benefit to the patient from a stenting therapy. The hemodynamic index is derived from a functional relation between the translesional pressure indicator (TPI) and lumen volume reduction (S) through a parametric deterioration of the RAS. Our in-house computational platform, *InVascular*, for image-based computational hemodynamics is used to compute the TPI at given S . *InVascular* integrates unified computational modeling for both image processing and computational hemodynamics with graphic processing unit parallel computing technology. The TPI- S curve reveals a pair of thresholds of S indicating mild or severe RAS. The TPI at $S = 0$ represents the pressure improvement following a successful stenting therapy. Six patient cases with a total of 6 aortic and 12 renal arteries are studied. The computed blood pressure waveforms have good agreements with the in vivo measured ones and the systolic pressure is statistical equivalence to the in-vivo measurements with $p < .001$. Uncertainty quantification provides the reliability of the computed pressure through the corresponding 95% confidence interval. The severity assessments of RAS in four cases are consistent with the medical practice. The preliminary results inspire a more sophisticated investigation for real medical

Abbreviations: AA, aortic artery; CTA, computed tomographic angiography; DR, diameter reduction; DSA, digital subtraction angiography; DUS, Doppler ultrasound; FFR, fractional flow reserve; FOSM, first-order second moment; GPU, graphic processing unit; ICH, image-based computational hemodynamics; LRA, left renal artery; MAP, mean arterial pressure; PDF, probability density function; RAS, renal arterial stenosis; RRA, right renal artery; TPI, translesional pressure indicator; TSPG, trans-stenotic pressure gradient; UQ, uncertainty quantification; VLB, volumetric lattice Boltzmann method; VR, volumetric reduction; WK3, 3-element WindKessel model.

This is an open access article under the terms of the [Creative Commons Attribution-NonCommercial](https://creativecommons.org/licenses/by-nc/4.0/) License, which permits use, distribution and reproduction in any medium, provided the original work is properly cited and is not used for commercial purposes.

© 2022 The Authors. *International Journal for Numerical Methods in Biomedical Engineering* published by John Wiley & Sons Ltd.

Rou Chen, College of Metrology and Measurement Engineering, China Jiliang University, Hangzhou, China

Funding information

National Science Foundation, Grant/Award Number: CBET1803845; PI4D; RITDP; University Fellowship of IUPUI; XSEDE, Grant/Award Number: ACI-1548562

insights of the new index. This computational concept can be applied to other arterial stenoses such as iliac stenosis. Such a noninvasive and patient-specific hemodynamic index has the potential to aid in the clinical decision-making of interventional treatment with reduced medical cost and patient risks.

KEYWORDS

image-based computational hemodynamics, noninvasive and patient-specific assessment, renal arterial stenosis, uncertainty quantification, volumetric lattice Boltzmann method

1 | INTRODUCTION

Renal arterial stenosis (RAS) has been known to be one of the primary contributors to elevated renal resistance.¹ It may cause reduced juxtaglomerular blood pressure in the kidney,² resulting in renovascular hypertension that may further induce direct kidney failure in synergy with the harmful effects of diabetes if present.³ Noninvasive imaging modalities have been popularly used to guide endovascular therapy for RAS in the clinic.⁴ Doppler ultrasound (DUS) is the safest and least expensive but also the least accurate method of assessment. It heavily relies on the skill of the sonographer, the body habitus of the patient, and the presence of bowel gas. It has been an appropriate initial choice for the diagnosis of RAS. Computed tomographic angiography (CTA) is the next option to assess the percentage of lumen diameter reduction (DR) via visual estimation but it can only provide the anatomical abnormalities of the arterial lumen without hemodynamic insight. Although RAS has been popularly diagnosed by DUS and CTA, the determination of benefit to a patient from therapeutic intervention, such as stenting or bypass, remains challenging. The last two reported and largest randomized trials, angioplasty and stenting for renal artery lesions (ASTRAL)⁵ and cardiovascular outcomes in renal atherosclerotic lesions (CORAL),^{6,7} of percutaneous renal artery intervention, have generated much debate and controversy⁸ as both have not been able to demonstrate clinical benefits from stenting therapy for patients with RAS. The reason may be from the design flaws⁹ in the trials including variability in inclusion and exclusion criteria, inconsistent definitions of improvement, mixtures of hypertension, and renal function endpoints, making the selection of patients for renal artery stenting a controversial topic. For example, the stenosis severity criterion, which was 60%¹⁰ of the lumen DR, may be inappropriate.

Practical means for noninvasive assessment of the true hemodynamic severity caused by RAS are currently lacking in clinical practice. A gold standard is only available for coronary arterial stenosis, for which the fractional flow reserve (FFR) is used to determine the severity of myocardial ischemia.¹¹ FFR is defined as the ratio of the distal pressure P_d to the proximal pressure P_a of the coronary stenosis; namely, $FFR = P_d/P_a$. The clinical guideline is as follows: $FFR < 0.75$ indicates significant coronary stenosis; $FFR > 0.8$ suggests insignificant coronary stenosis; and if $0.75 < FFR < 0.8$, the severity assessment requires additional pathophysiological information. While FFR is a reliable hemodynamic index for coronary arterial stenosis, its clinical application is rather limited¹² due to (a) the cumbersome nature of invasive pressure measurement via catheterization, (b) the risk of medical and surgical complications, and (c) the high cost of guidewires and measurement. Meanwhile, the applicability of FFR for noncoronary arterial stenoses remains questionable due to the different flow reserves in different vascular beds. For example, the vasodilatory reserve (the maximum increase in blood flow through the artery above the normal resting volume) in the coronary circulation is 4–5 times baseline, whereas it may go up to 80 times in some peripheral circulation beds.¹³ There have been attempts to determine the effectiveness of renal FFR for quantifying the functional significance of RAS but the FFR thresholds are not uniform.^{14–19}

Evidence has shown that hemodynamic severity is present where a significant pressure gradient across a RAS exists.²⁰ Since a decrease in renal pressure distal to the stenosis is the fundamental trigger of renovascular hypertension, measurement of the trans-stenotic pressure gradient (TSPG) would perhaps provide a more appropriate means of assessing renal resistance.²¹ TSPG is defined as the pressure drop between the aortic (proximal) and renal (distal) artery across the RAS, referred to as $TSPG = P_a - P_d$. There has been a consensus that a resting peak systolic pressure gradient > 20 mmHg is significant in RAS, but it has not been clinically proven.²² It remains to be evaluated either TSPG or FFR is more appropriate to evaluate the functional hemodynamics in the aortorenal vascular bed but, so far, no consensus has been made. Since either FFR or TSPG is calculated from the proximal and distal pressures to the stenosis, that is, P_d and P_a , the important questions become how P_d and P_a can be noninvasively quantified and how they can be used

to establish standard guidelines for assessing the hemodynamic severity of RAS. In what follows, we use a translesional pressure indicator (TPI) to represent FFR and/or TSPG. The pressure can be systolic pressure (p_{sys}), diastolic pressure (p_{dia}), or mean arterial pressure (MAP). The MAP represents the average arterial pressure throughout one cardiac cycle. The common formula to calculate MAP is $p_{\text{dia}} + (p_{\text{sys}} - p_{\text{dia}})/3$.

Due to the advances in medical imaging, computational power, and mathematical algorithms, image-based computational hemodynamics (ICH) has emerged to noninvasively quantify 4-D (space + time) hemodynamics in the human heart and major blood vessels based on patient's CTA and DUS data. This new potential gives rise to a promising field of medical diagnostics and therapeutics in a patient-specific environment.^{23–27} Computational data obtained from ICH are not readily available from the current standard clinical measurements, which may offer key insights into disease progression and subsequent physiological response, thus aiding in clinical decision-making for various cardiovascular diseases.^{28–33} For example, FFR-CT²⁸ computed from ICH has been a promising substitute for the functional evaluation of coronary stenosis²⁹ with a growing body of evidence for diagnostic accuracy compared with the invasive FFR.

In this work, we develop a new noninvasive and patient-specific hemodynamic index for assessing the hemodynamic severity of RAS, using ICH and related computational derivatives. An in-house computational platform, named *InVascular*,²⁷ is used. *InVascular* synergistically integrates the lattice Boltzmann method^{34,35} for both image segmentation and computational fluid dynamics with emerging graphics processing unit (GPU) parallel computing technology,^{36–38} resulting in exceptionally fast computation speed. The key of this work is to establish a patient-specific functional relationship between TPI and S through a virtual deterioration of RAS, of which S is the degree of stenosis measured by either diameter or volume reduction of the arterial lumen, see definition in Section 2.2. The hemodynamic index is then derived from the TPI– S curve to determine the hemodynamic severity of existing stenosis, either mild, severe, or in between based on two thresholds of the S . Meanwhile, the TPI at $S = 0$ provides a baseline prediction of the pressure improvement after a potential interventional treatment. To establish the TPI– S curve, we need to execute *InVascular* repeatedly. For example, varying the lumen reduction from 0% to 95% with an increment of 5% results in 20 executions for one case. Thus, fast computation is critically important to establish the hemodynamics relation between TPI and S .

2 | METHOD AND MATERIALS

The computational concept generally involves four components from medical imaging data to the assessment of RAS severity, as depicted in Figure 1. First, *image extraction* provides the 3-D anatomical geometry of the stenosed aortorenal arterial system from CTA with existing stenosis (S_e) and the velocity waveform from DUS at inlet and outlets for boundary conditions. Second, the *GPU-accelerated volumetric lattice Boltzmann method* (VLBM)³⁴ solver computes the 4-D hemodynamics in the arterial system, from which the TPI at S_e is obtained. Third, *parametric deterioration* of the existing stenosis from 0% to 95% with an increment of 5% results in a relationship between TPI and S , along which two thresholds of parametric RAS degree, S_m for mild and S_s for severe stenosis, are revealed. Fourth, the *hemodynamic severity* of the RAS is assessed through the comparison of S_e with S_m and S_s and the potential improvement of pressure can be predicted from the TPI at $S = 0$. In addition, we perform an uncertainty quantification (UQ) analysis to demonstrate the reliability of the ICH.

2.1 | Computation of TPI in image-based aortorenal arterial systems using *InVascular*

We use *InVascular* to compute the TPI based on imaging data. The detailed methods of *InVascular* including image segmentation, VLBM solver, inlet and outlet boundary conditions, and GPU parallelization are referred to references [34, 37, 39, 40]. Here we consolidate the major components for the completion of this presentation. As shown in Figure 2, the inputs of the VLBM solver include the anatomical geometry of the aortorenal arterial system, the physical and computation quantities, and inlet and outlet boundary conditions. Its output is the 4-D hemodynamics in the aortorenal arterial system, from which the TPI is calculated. The aortorenal arterial system is represented by the volumetric parameter field $\mathcal{P}(\mathbf{x})$, defined in the following sections. In this work, we use Materialize Mimics, for the convenience to deal with the parametric deterioration of the RAS (described in Section 2.2), to extract the anatomical geometry of the aortorenal arterial system from patient's CTA and save the image segment in STL format. Then we calculate the $\mathcal{P}(\mathbf{x})$ field using our in-house Matlab code.³⁹

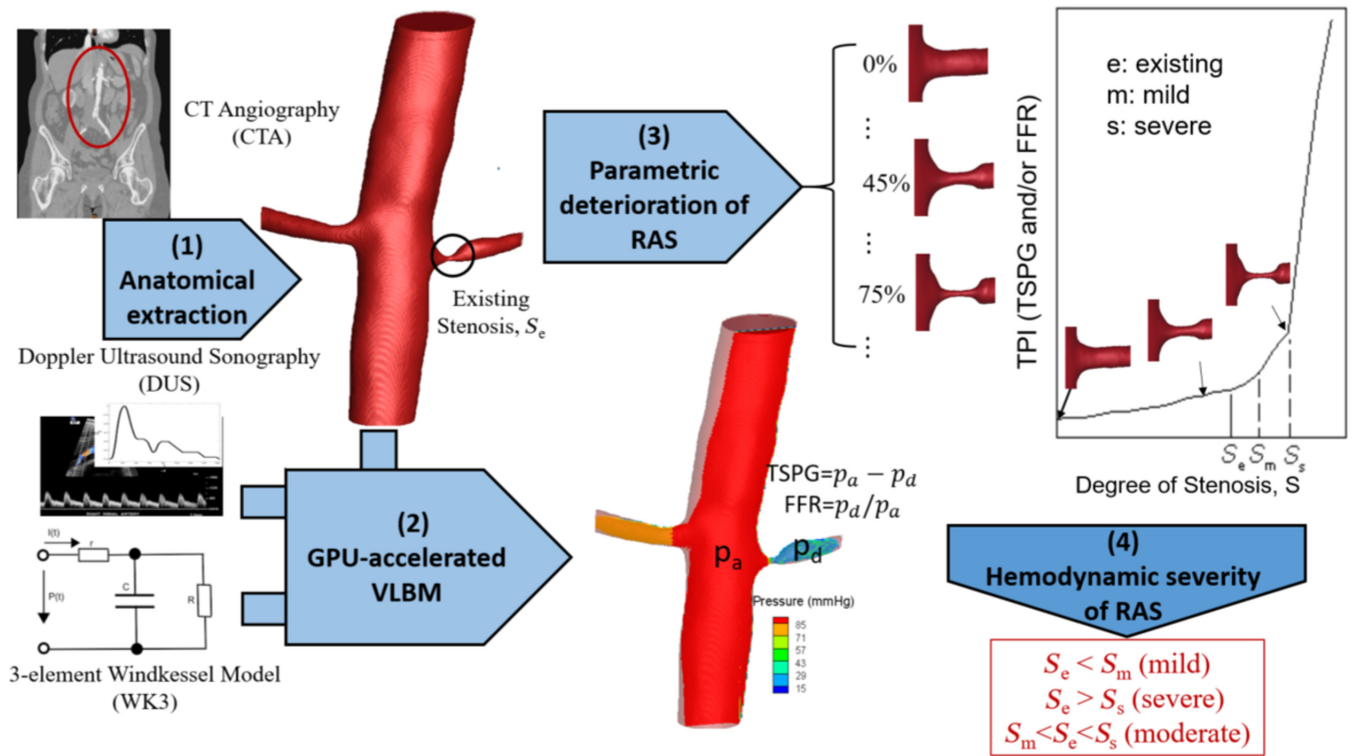


FIGURE 1 Schematic diagram of the computational concept to assess hemodynamic severity of RAS from medical imaging data: (1) image extraction, (2) GPU-accelerated VLBM solver, (3) parametric deterioration of RAS to establish TPI-S relation, and (4) hemodynamic severity determined by two thresholds of the parametric RAS degree, S_m (mild) and S_s (severe)

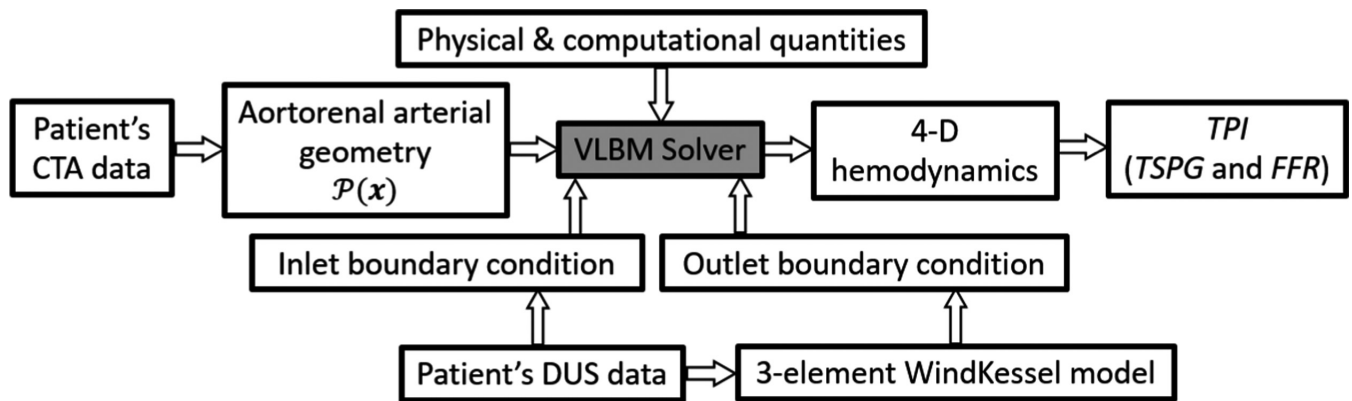


FIGURE 2 Schematic diagram of *InVascular*. The core is a VLBM solver with its inputs of the anatomical geometry of the aortorenal arterial system, the physical and computation quantities, and inlet and outlet boundary conditions and the outputs is the 4-D hemodynamics where the TPI is calculated.

The VLBM³⁴ is a volumetric representation of the lattice Boltzmann method. In VLBM, fluid particles are uniformly distributed in lattice cells as opposed to sitting at lattice nodes in the conventional lattice Boltzmann method. As shown in Figure 3, when an arbitrary boundary (black line) separates a fluid domain (without dots) from a solid boundary structure (with dots), three distinct cells are characterized through the volumetric parameter $\mathcal{P}(\mathbf{x})$, defined as the occupation of solid volume $\Delta V_s(\mathbf{x})$ in the cell with total volume $\Delta V(\mathbf{x})$, that is, $\mathcal{P}(\mathbf{x}) \equiv \Delta V_s(\mathbf{x})/\Delta V(\mathbf{x})$. They are fluid cell ($\mathcal{P} = 0$), solid cell ($\mathcal{P} = 1$), and boundary cell ($0 < \mathcal{P} < 1$).

On a lattice space with b directions of discrete molecular velocity, VLBM deals with the time evolution of the particle population, $n_i(\mathbf{x}, t)$, corresponding to the i th velocity \mathbf{e}_i

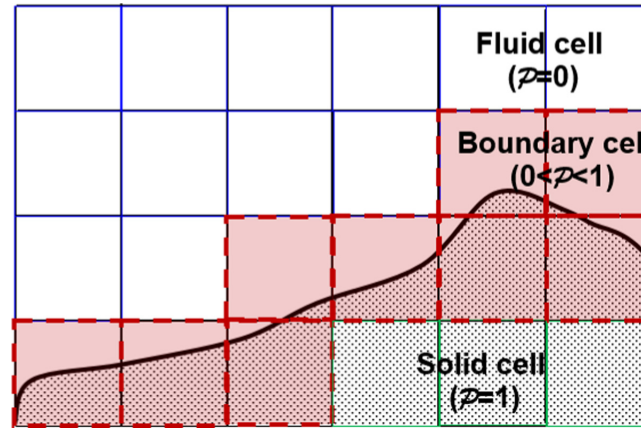


FIGURE 3 Three types of lattice cells in VLBM: fluid cell ($\mathcal{P}=0$), solid cell ($\mathcal{P}=1$), and boundary cell ($0 < \mathcal{P} < 1$). The solid line represents an arbitrary boundary of the flow domain.

$$n_i(\mathbf{x} + \mathbf{e}_i \delta t, t + \delta t) = n_i(\mathbf{x}, t) - \frac{[n_i(\mathbf{x}, t) - n_i^{\text{eq}}(\mathbf{x}, t)]}{\tau}, i = 0, \dots, b \quad (1)$$

where $n_i^{\text{eq}}(\mathbf{x}, t)$ and τ are the corresponding equilibrium particle population and relaxation time, respectively. The resulting density $\rho(\mathbf{x}, t)$ and velocity $\mathbf{u}(\mathbf{x}, t)$ in the fluid domain are

$$\rho(\mathbf{x}, t) = \sum n_i(\mathbf{x}, t) / [1 - \mathcal{P}(\mathbf{x}, t)] \text{ and } \mathbf{u}(\mathbf{x}, t) = \sum \mathbf{e}_i n_i(\mathbf{x}, t) / \sum n_i(\mathbf{x}, t). \quad (2)$$

The pressure field $p(\mathbf{x}, t)$ is then calculated from

$$p(\mathbf{x}, t) - p_0 = c_s^2 [\rho(\mathbf{x}, t) - \rho_0], \quad (3)$$

where p_0 and ρ_0 are reference pressure and density, respectively.

Equation (1) consists of three operations: (1) *collision* taking into account the momentum exchange between the willfully moving boundary and the flow, (2) *streaming* accompanying a volumetric bounce-back procedure in boundary cells, and (3) *boundary-induced volumetric fluid migration* moving the residual fluid particles into the flow domain when the boundary swipes over a boundary cell toward a solid cell. The detailed formulae are found in the publications.^{34,39} In this work, we treat static arterial walls thus no momentum exchange between the arterial wall and the blood flow is accounted for. The VLBM can handle arbitrary oriented boundaries with or without motion, and it satisfies mass conservation strictly. The formulation, taking into consideration of moving boundary (if applied) and bounce-back boundary conditions, is self-regulated by the volumetric parameter field $\mathcal{P}(\vec{x})$. This feature provides an advantage to deal with the parametric deterioration of stenosis for establishing the TPI- S relation, presented in the following sections.

We introduce velocity and pressure boundary conditions at the inlet and outlets⁴⁰ of the aortorenal arterial system, respectively. A pulsatile paraboloidal velocity profile is constructed based on patient's DUS velocity waveform at the inlet to drive the blood into the arterial systems. The velocity profile fits the real shape of the arterial lumen. At each outlet, a pulsatile pressure is calculated at each time step of the simulation through the three-element WindKessel model (WK3)^{41,42} to capture the effects of the global blood circulation on the blood flow in the segmented arterial domain. The DUS velocity waveforms are used to tune the r , C , and R values in the WK3 model at each outlet. As shown in Figure 4, the WK3 adopts a Windkessel circuit to model one capacitor (C) that represents the vessel compliance, and two resistors (r and R), representing the proximal and distal flow resistances, respectively. The detail algorithms for the inlet and outlet boundary conditions are found in the reference [40].

In the VLBM, we employ the nonequilibrium extrapolation boundary condition⁴³ as follows.

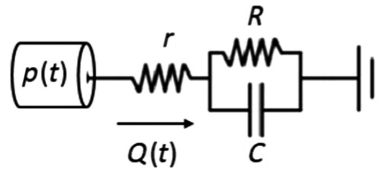


FIGURE 4 WK3 model consists of one capacitor (C), modeling vessel compliance and two resistors (r and R) modeling proximal and distal resistance respectively.

$$n_i(\mathbf{x}_b, t) - n_i^{\text{eq}}(\mathbf{x}_b, t) = n_i(\mathbf{x}_f, t) - n_i^{\text{eq}}(\mathbf{x}_f, t), \quad (4)$$

for i th direction where \mathbf{x}_b and \mathbf{x}_f are the boundary cell and its next fluid cell along that direction, respectively. If the velocity, $\mathbf{u}(\mathbf{x}_b, t)$, is known at the boundary cell, the *velocity boundary condition* is

$$n_i(\mathbf{x}_b, t) = n_i^{\text{eq}}(\rho(\mathbf{x}_f, t), \mathbf{u}(\mathbf{x}_b, t)) + n_i(\mathbf{x}_f, t) - n_i^{\text{eq}}(\mathbf{x}_f, t). \quad (5)$$

whereas if the pressure $p(\mathbf{x}_b, t)$ is given at the boundary cell, the *pressure boundary condition* reads

$$n_i(\mathbf{x}_b, t) = n_i^{\text{eq}}(\rho(\mathbf{x}_b, t), \mathbf{u}(\mathbf{x}_f, t)) + n_i(\mathbf{x}_f, t) - n_i^{\text{eq}}(\mathbf{x}_f, t), \quad (6)$$

where $\rho(\mathbf{x}_b, t)$ is calculated from Equation (4). We use the velocity and pressure boundary conditions at the inlet and outlet(s), respectively.

The VLBM has been fully CUDA-GPU parallelized.^{36–38,44} Quantifying the 4-D hemodynamics in a typical human artery system, for example, aortoiliac artery, with a resolution of $94 \times 145 \times 256$ takes 26.4 h (wall-clock) on central processing unit (Intel(R) Xeon(R) X5660). With the parallel computing on GPU (Tesla C2075), the computation time reduces to 0.1 h, resulting in 264 times speedup. Such an acceleration is critical to enable the establishment of the TPI– S relation for the new hemodynamic index, which requires executing the VLBM solver 20 times for each patient case.

2.2 | Derivation of the hemodynamic index for the severity of RAS

For a noncoronary arterial stenosis, one cannot determine the hemodynamic severity of an existing RAS, confined by solid and solid lines in Figure 5A, based on the value of TPI. To determine the hemodynamic severity, we construct a parametric deterioration of the RAS by varying the lumen reduction S from 0% to 95% with an increment of 5%, confined by the solid and dashed lines in Figure 5A. As shown in Figure 6, we manually deteriorate the stenosis using Materialize Mimics, the same software we use to extract the anatomic arterial system from the patient's CTA. We first select the local arterial segment that contains the stenosis, the area confined by the dash lines. Flattening the local artery results in the 0% degree of the stenosis. We define the corresponding volume and diameter of the local segment as V_0 and D_0 , respectively. Then we deteriorate the stenosis by shrinking the arterial lumen to volume V and diameter D . We use two ways to express the degree of the stenosis: either DR, $= D/D_0$, or volumetric reduction (VR), $S = V/V_0$. Noticing that the cross-section of a human artery is not circular in general, we always use the smallest diameter to calculate the DR. For a parametric deterioration, we do not look closely at the orientation of the diameter and the 3-D shape of the stenosis but just focus on the value of the diameter and the volume. We try to smooth the parametric artery walls. At each degree of stenosis (S), the software generates a new STL file for the aortorenal arterial system with the parametric stenosis. Our in-house Matlab code calculates the volumetric parameter field $\mathcal{P}(\mathbf{x})$, which is fed into the VLBM solver to compute the corresponding TPI by keeping the flow conditions the same. Repeating the TPI computation for each parametric stenosis, see Figure 5B, we obtain a functional relation between TPI and S as shown in Figure 5C. The TPI– S curve provides two important diagnostic and therapeutic insights. First, two thresholds, S_m and S_s , can be identified based on the local fitting curve slopes, see dashed lines Figure 5D. These two critical S values form the hemodynamic index. It is noted that the determination of the thresholds of S_m and S_s is conceptual in this work based on the engineering concept. A clinical trial with a large number of patient cases is necessary to derive the patient-specific thresholds with medical insights.

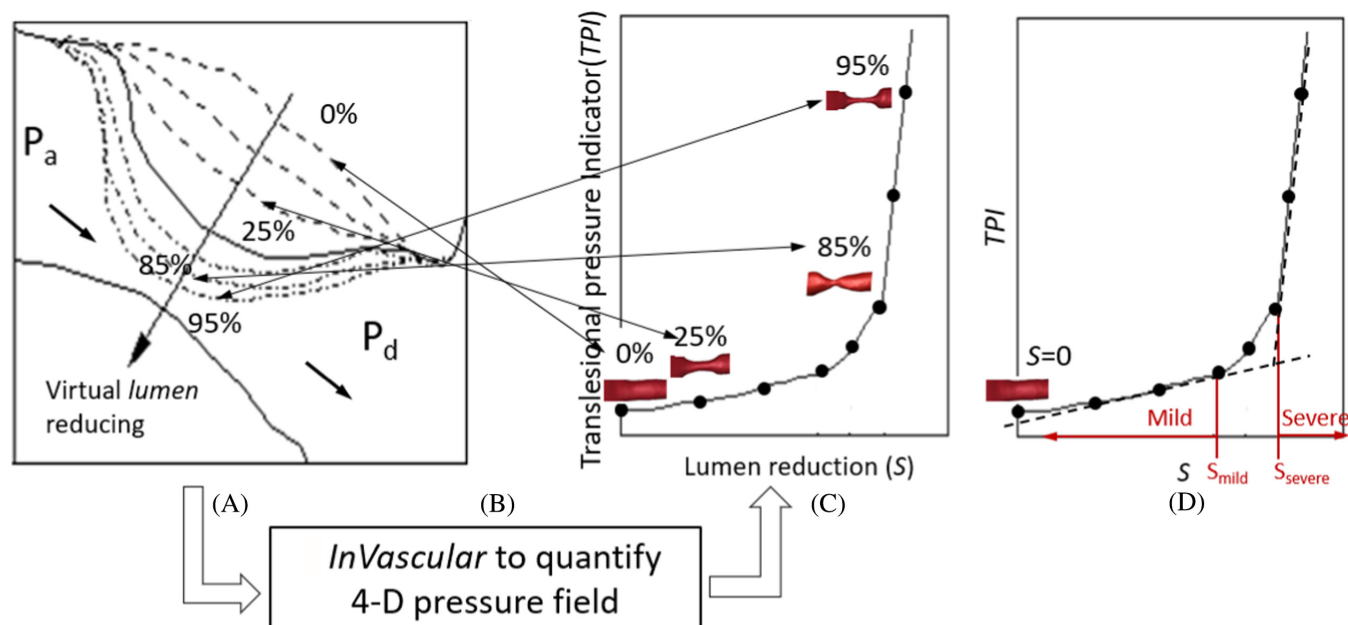


FIGURE 5 Schematic process for establishing the functional relation between TPI and S. (A) Virtual progression (solid-dashed lines) of an existing RAS (solid-solid lines) varying S from 0% to 95% with an increment of 5%, (B) VLBM computation of TPI for each level of S, (C) functional relation between TPI and S, and (D) two S thresholds, based on the slopes of TPI-S curve, for determining the severity of the existing RAS. The aortorenal artery system at $S = 0$ corresponds to the base morphology after an interventional treatment.

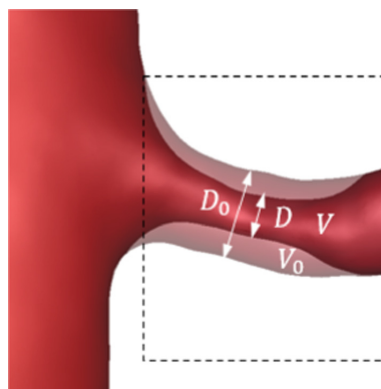


FIGURE 6 Two ways to define the lumen reduction (S): either diameter reduction $S = D/D_0$ or volume reduction $S = V/V_0$

Placing the existing stenosis level, S_e , on the TPI-S curve, one can determine the severity of the RAS as mild if $S_e < S_m$, severe if $S_e > S_s$, and moderate stenosis if $S_m < S_e < S_s$. Compared to the single TPI value, the TPI-S curve delivers richer hemodynamic information that enables an assessment of the severity of RAS. A guideline for patient management in terms of the benefits of an interventional treatment can be derived as follows:

- If the RAS is mild ($S_e < S_m$), no interventional treatment is needed.
- If the RAS is severe ($S_e > S_s$), interventional treatment is beneficial.
- If the RAS is moderate ($S_m < S_e < S_s$), medical management with additional pathophysiological information to determine whether intervention would be beneficial.

Meanwhile, as seen in Figure 5D, TPI at $S = 0$ represents the pressure condition after a stenting therapy. It can be used as a baseline prediction of the benefit to the patient for a severe RAS from an interventional treatment. In clinical practice, stenting may not always result in $S = 0$. Sometimes, the stenosis might be over-stretched resulting in negative

S , corresponding to which the TPI can be computed directly from *InVascular* or through extrapolation from the TPI- S curve. Thus, baseline prediction may include a range of TPI corresponding to a range of S in practice.

The lumen reduction (S) is referred to as either DR or VR. While DR (one dimension) has been heavily used in the current clinical practice because it can be easily measured from radiological imaging, VR (three dimensions) is thought to be more appropriate to characterize the degree of stenosis since the blood flow and morphological shape of stenosis are 3-D.

2.3 | UQ for the reliability of ICH

Uncertainty exists in the entire process of deriving the patient-specific hemodynamic index from the patient's imaging data. Sources of uncertainty start from the acquisition of images through the determination of the two thresholds of S on the TPI- S curve.⁴⁵⁻⁴⁷ Uncertainty can be from the randomness in image acquisition, the skill of the sonographer, the body habitus of the patient, radiation dose, contrast quality, and many parameters involved in *InVascular*. The randomness in background noise, calcification, and color discontinuity for CTA, inaccurate location, and unstable wave cycles for DUS may affect the extraction of the blood flow domain and the flow information at the inlet and outlet(s). In computational modeling, uncertainty may exist in the inlet/exit boundary conditions, vessel wall model, flow model, and limitations in the resolution. Since uncertainty is inevitable, a question arises about how reliable the patient-specific hemodynamic index is toward clinical use.

Uncertainty is usually analyzed by the probability theory.⁴⁸⁻⁵⁰ For instance, if uncertainty is associated with a parameter, for example, DR of arterial lumen measured from CTA, it is commonly modeled as a random variable. The randomness can be fully characterized by its probability density function (PDF) that determines the feature of the randomness, such as normal, lognormal, and Weibull distributions. From the PDF, one can quantify the uncertainty from the mean and SD of the random variable. If multiple random variables are involved, such as r , C , and R parameters in the WK3 model, a joint PDF will be used. UQ is critically important for risk assessment and patient management when the patient-specific hemodynamic index is used in clinical practice.

UQ treats *InVascular* as a black box with random input variables and random outputs of interested quantities. The purpose of UQ is to quantify the effects of the model input uncertainty on the model output, which has been widely used in engineering and other fields for reliability analysis,⁵¹⁻⁵⁴ robustness assessment,⁵⁴⁻⁵⁶ and risk mitigation.^{57,58} In this study, the model of *InVascular* is given by $\mathbf{y} = g(\mathbf{x})$, where \mathbf{x} is the model input, which contains input variables, such as parameters to characterize the boundary condition, and \mathbf{y} is the model output, such as the pressures to be calculated.

The random inputs on which this study focuses include the r , C , and R parameters, which are the components of \mathbf{x} , in the WK3 model. They have significant effects on the model outputs. The parameters are assumed independently and normally distributed.

UQ is performed by the first-order second moment (FOSM) method,⁵⁹⁻⁶¹ which is a common UQ method in engineering. FOSM linearizes $g(\mathbf{x})$ at the means of \mathbf{x} . Given the normally distributed input variables, the outputs of the approximated $g(\mathbf{x})$ are also normally distributed, and they can be modeled by a multivariate normal distribution. FOSM is used because it is efficient for UQ for this study. Unlike a sampling-based UQ approach which needs to call $g(\mathbf{x})$ many times (for instance, $10^2 - 10^5$ times), FOSM calls $g(\mathbf{x})$ only $n + 1$ times, where n is the dimensionality of \mathbf{x} . Calling $g(\mathbf{x})$ or *InVascular* is computationally expensive, and it is desirable to minimize the number of function calls.

The steps of FOSM are as follows. At first, the means and SD s of \mathbf{x} are determined from the data. Then $g(\mathbf{x})$ is linearized at the means of \mathbf{x} with the first-order Taylor expansion. The means and covariances of the model output \mathbf{y} are obtained.

The joint distribution of \mathbf{y} provides more valuable information than the deterministic analysis. For instance, instead of having a single value of a computed pressure without consideration of uncertainties, more information is available about the pressure. The mean of the pressure gives the best estimate of the pressure, and the SD provides the associated uncertainty. The pressure can also be alternatively reported in the form of $y = \bar{y} \pm U_y$, where \bar{y} is the best estimate of the pressure, and U_y is the uncertainty term under a certain confidence level, such as 95%. We can then state that the actual pressure is between $\bar{y} - U_y$ and $\bar{y} + U_y$ with a probability of 0.95. Such quantitative analysis provides the reliability of the computed pressure and the confidence in the derived hemodynamic index.

2.4 | Study cases

Six patient cases are studied. All the patients are male and their ages are from 64 to 87. The imaging data including CTA and DUS were obtained from the electronic medical libraries in Indiana University Methodist Hospital in Indianapolis, IN, USA (Cases I and II), and Hangzhou First People's Hospital, Hangzhou, China (Cases III–VI). IRB approval (#1309233521R003 | N) was obtained for the patients enrolled from Indiana University. The study (#116-01) was approved by the Ethics Committee of Hangzhou First People's Hospital. It only involved a retrospective analysis of clinically indicated procedures; therefore, informed consent was not required. The investigation conformed to the principles outlined in the Declaration of Helsinki. The CTA resolution is approximately $0.75^2 \times 2.5 \text{ mm}^3$ (Cases I and II) and $0.65^2 \times 0.6 \text{ mm}^3$ (Cases III–VI). Among the six cases, Cases I–V have the invasive pressure measurements in the aortic artery (AA), left renal artery (LRA), and right renal artery (RRA) during digital subtraction angiography (DSA) for interventional treatments. These invasively measured pressure waveforms are used to validate the corresponding computed ones. The pulsatile pressure waveform in AA (P_{AA}) was measured directly with a catheter placed in the aorta and a pressure transducer. Pressure waveforms in RRA (P_{RR}) and LRA (P_{LR}) were measured with a pressure wire advanced at least 4 cm distal to the RAS under resting conditions. The measurements were repeated after a renal artery vasodilator infusion of 30 mg of Papaverine. The complete pressure waveform was recorded over three cardiac cycles for each location. Cases II, with no RAS, and I were collected only for validating the computed pressure. The pressure measurements for these two cases were made when the patient underwent renal artery stent placement for fenestrated aortic aneurysm repairs. In Cases III–VI, RASs were observed, followed by DSA assessment to determine if stenting was needed. Among these four cases, Cases V and VI underwent a stenting procedure. In Case V, the invasive pressure measurement was done before and after stenting. Six patient cases with a total of 6 aortic and 12 renal arteries are involved for statistical analysis and UQ analysis. In Table 1, columns 2–5 are from medical notes, and columns 6 and 7 are the segmented aortorenal arterial system.

2.5 | Computational setup

Figure 7 shows the anatomical geometry of each aortorenal arterial system, extracted from the corresponding patient's CTA using Materialize Mimics. In the simulation, the blood density and kinematic viscosity, $1.06 \times 10^3 \text{ kg/m}^3$ and $3.3 \times 10^{-6} \text{ m/s}^2$, respectively, the dimensionless relaxation time $\tau (= 0.5079)$ in Equation (1), and the rigid arterial walls remain the same for all the cases. The physiological boundary conditions at the inlet and outlets are case to case. Here we list the r , C , and R values used at the outlets of AA, LRA, and RRA, respectively, in Table 2.

3 | RESULTS

We present preliminary results in this section. We first demonstrate the reliability of the computed pressure through the comparisons of computed vs. measured pressure and UQ analysis. Then, we show results related to the new hemodynamic index from individual cases as indicated. Although many different uncertainties exist, we focus on one

TABLE 1 Patient cases

Case	Existence of RAS	Stenting therapy	Pressure measurement	Heart rate (per min)	Physical size (cm^3)	Spatial resolution
I	No	No	Yes	83	$7.56 \times 6.11 \times 9.38$	$178 \times 144 \times 221$
II	No	No	Yes	78	$7.79 \times 6.31 \times 9.16$	$205 \times 166 \times 241$
III	Minor	No	Yes	87	$5.95 \times 4.69 \times 9.56$	$170 \times 134 \times 273$
IV	Minor	No	Yes	74	$6.37 \times 4.26 \times 10.07$	$172 \times 115 \times 272$
V	Severe	Yes	Yes	62	$7.48 \times 5.93 \times 11.39$	$192 \times 152 \times 292$
VI	Severe	Yes	No	64	$6.51 \times 4.34 \times 9.28$	$186 \times 124 \times 265$

Note: Columns 2–5 are from medical notes. Columns 6 and 7 are the segmented aortorenal arterial system.

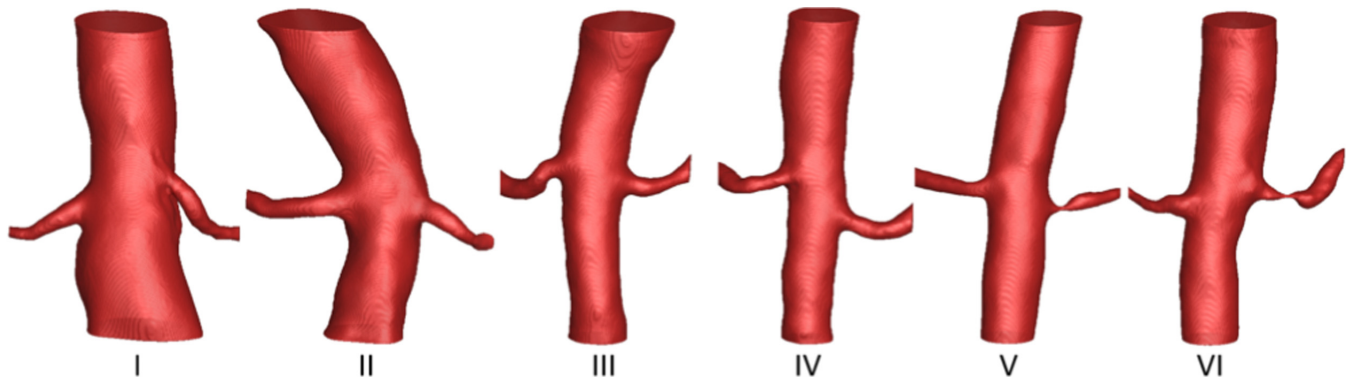


FIGURE 7 Anatomical extracted aortorenal artery systems from patient's CTA images. The physical domains are listed in Table 1.

TABLE 2 Proximal resistance r , compliance C , and distal resistance R used in WK3 at AA, LRA, and RRA outlets

Case	r (dynes·s/cm ⁵)			$10^{-5}C$ (cm ⁵ /dynes)			R (dynes·s/cm ⁵)		
	AA	LRA	RRA	AA	LRA	RRA	AA	LRA	RRA
I	88.0	2982.40	5972.8	1.80	0.36	0.32	2773.10	7666.03	15358.70
II	97.32	1399.88	6122.16	9.44	0.57	0.35	3053.08	3597.03	15742.70
III	87.99	3533.04	5412.88	1.80	0.36	0.32	2773.10	9105.91	13918.85
IV	108.12	2879.76	3306.39	1.00	0.54	0.48	3386.38	7386.06	8505.96
V	97.32	1399.88	6122.16	9.44	0.57	0.35	3053.08	3597.03	15742.70
VI	150.00	3093.07	3173.02	4.72	0.35	0.54	5039.01	7959.34	8159.01

uncertainty in this preliminary application. We only analyze the effects of r , C , and R selection in WK3 on the computed pressure.

3.1 | Reliability of noninvasively computed pressure using *InVascular*

The reliability of the computed pressure is demonstrated in two aspects. The first is the closeness of the noninvasively computed pressure to the invasively measured pressure. The second is the range of computed pressure within which the true pressure is asserted to lie with a 95% confidence interval.

3.1.1 | Computed versus measured pressure in one cardiac cycle

Figure 8A shows the comparisons of the pressure waveform in one cardiac cycle between noninvasive computation (solid lines) and invasive measurement (dashed lines with symbols) for Case I in AA (red), LRA (green), and RRA (blue). The computed pressure waveforms agree with the measured ones in general, with better agreement at systolic pressure than diastolic pressure. Statistical analysis for Cases I–V including 14 artery samples demonstrates the statistical equivalence between the computed and measured systolic pressure. The mean computed systolic blood pressure matches exactly the in vivo measured one, that is, 128 torr (mmHg). The mean difference between computed and measured systolic blood pressures was -0.14 torr (mmHg) + 0.32 torr (mmHg). There was no difference in these values by the paired t -test ($p = .123$), with a value greater than 0.05, implying no statistical difference. As shown in Figure 8B, the Bland–Altman plot of the data shows that, among the 14 arteries, only one measurement falls minimally outside the 95 percent confidence interval. The calculated systolic blood pressure was correlated with the measured one with a correlation coefficient of 1 ($p < .001$) and the Beta value for a linear regression analysis was 0.003, demonstrating a consistent correlation between the systolic pressure at all measurements.

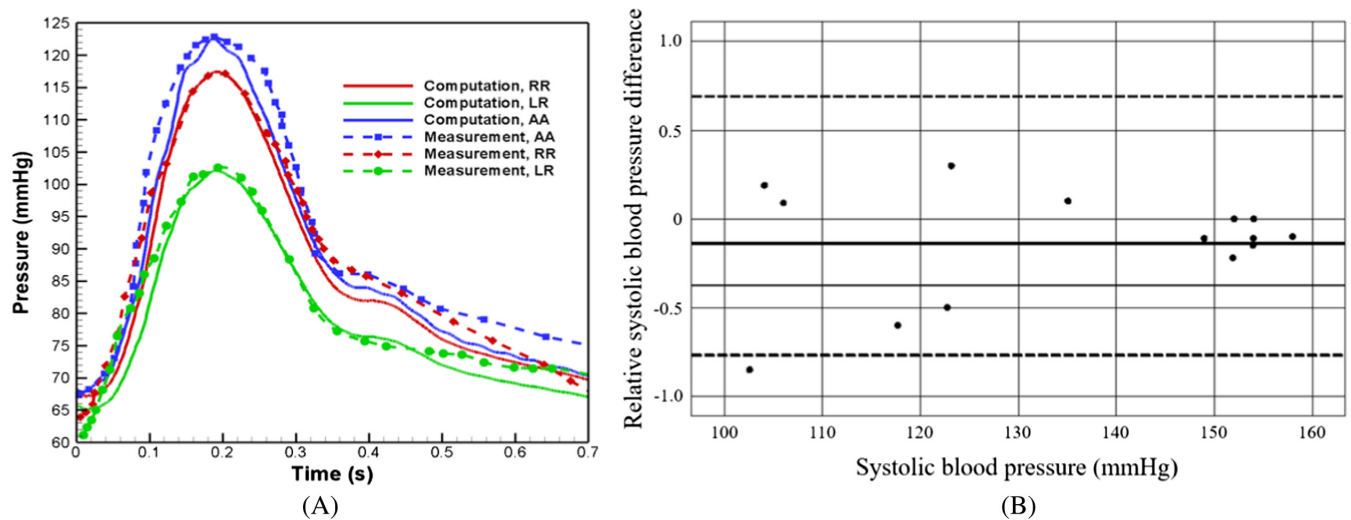


FIGURE 8 (A) Noninvasively computed (solid lines) versus invasively measured (dashed lines with symbols) pressure waveforms for Case I in AA (red), LRA, (green), and RRA (blue). (2) Bland-Altman plot of 95% confidence for systolic blood pressure differences. Five cases of I-V including 14 AA, LRA, and RRA samples were used for the statistical analysis. There was no statistical difference between computed and measured systolic blood pressure by the paired t -test ($p = .123$), with a value greater than 0.05.

TABLE 3 95% Confidence intervals of computed systolic pressure in mmHg of five cases

Case	95% Confidence interval			Computed pressure		
	P_{AA}	P_{LR}	P_{RR}	P_{AA}	P_{LR}	P_{RR}
I	[121, 125]	[100,105]	[116, 119]	123	102	117
II	[108, 112]	[73,76]	[105,108]	111	74	106
III	[154, 160]	[151,157]	[150,155]	157	154	152
IV	[153, 159]	[142, 147]	[140, 144]	155	145	142
VI	[160, 168]	[56, 57]	[150, 158]	164	56	154

Note: Fourteen artery samples were used for this statistical analysis.

3.1.2 | UQ for the impact of boundary conditions on TSPG

The objective of UQ is to determine how likely the computed quantities would be if uncertainty is present in a flow system. As discussed in Section 2.3, there exist various uncertainty sources in the process to derive the hemodynamic index from the medical images. One of the major uncertainty sources comes from the WK3 model⁴¹ that is commonly used for the boundary conditions at the exits of the artery segment. The model involves three parameters r , C , and R as shown in Figure 1 at each exit. They are estimated iteratively by calling ICH to match the flow rate at the exit based on the DUS velocity waveform. Given the uncertainty, it is necessary to quantify its impact on pressure computation. Using r , C , and R as input variables and three computed pressure values at AA, LR artery, and RR artery as output variables, we performed UQ analysis for Cases I-V in Table 1 to demonstrate how the uncertainty of the input variables impacts the pressure computation. There are nine input variables for the three exits of AA, LR artery, and RR artery. The output variable is systolic pressure. The UQ is performed by the FOSM method.⁵⁹⁻⁶¹ The joint PDF of the three output variables is obtained and then the 95% confidence intervals of the output variables are derived. Table 3 shows the outcome of the UQ analysis for the 95% confidence intervals of systolic pressure in AA, LRA, and RRA. The uncertainty in an output variable is indicated by the width of the confidence interval. For instance, for Case I, $P_{AA} = [153,159]$ (mmHg), which indicates that the chance that the actual value of P_{AA} falling into the interval is 95%. The confidence interval can also be rewritten as $P_{AA} = \bar{P}_{AA} \pm U_{P_{AA}} = 156 \pm 3$ (mmHg) where $\bar{P}_{AA} = 156$ (mmHg) is the best estimate of P_{AA} , and $U_{P_{AA}} = 3$ (mmHg) represents the uncertainty associated with P_{AA} , which is caused by the uncertainty in the boundary conditions. For a general output variable y , the traditional scientific computation can only produce a single-valued

prediction of \bar{y} without the uncertainty term U_y . With the additional information (U_y), UQ can supply more information for the reliability of the output.

3.2 | Characterization of RAS degree: DR versus VR of the arterial lumen

Although DR is extensively used in current clinical practice to characterize the degree of stenosis, VR is more related to the impact of RAS on TPI given the fact that the blood flow is 3-D. We show one study on the LRA of Case VI in Table 4. Two parametric scenarios are shown: (left) varying the lumen VR from 38% to 60% for a RAS with fixed lumen DR (75%) and (right) varying the lumen DR from 53% to 69% for a RAS with fixed lumen VR (45%). The TSPG of each parametric stenosis is quantified by *InVascular*. In the left with a fixed DR, 1% VR causes a 0.66 mmHg increase of TSPG whereas, in the right with a fixed VR, 1% DR causes a 0.2 mmHg increase of TSPG, implying that the VR of the vessel lumen tracts closer to the hemodynamics than the shape of the cross-section characterized by DR. This result agrees with a previous computational analysis⁶² and our ongoing study on aortoiliac arterial systems. Thus, we use VR to establish the TSPG–S correlation below unless otherwise mentioned.



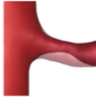



3.3 | Hemodynamic index derived from the functional relation of TPI–S

Parametric analysis was performed for Case VI, in which severe RASs, $S_e = 65\%$, in the LRA were observed from the CTAs, and stenting therapies were done in the clinical setting. From *InVascular*, the systolic TSPG and FFR-CT for the RAS were computed as 57.6 mmHg and 0.54, respectively. For determining the RAS severity, computational analysis was performed via a parametric deterioration of the RAS by increasing lumen volume reduction, S , from 0% to 80% with an increment of 5%. It is noted that 0% of lumen volume reduction represents the scenario of no remaining stenosis (after stenting). Through *InVascular* quantification, the correlations of systolic TSPG (left, solid line) and systolic FFR-CT (right, dashed line) versus S were established in Figure 9. Based on the local fitting slopes of the curve indicated by two dash-dot lines, two thresholds, S_m and S_s , are identified as 30% and 40%, respectively. The therapeutic guidelines for this RAS were determined as follows: If $S < 30\%$, no stenting is needed, and if $S > 40\%$, stenting therapy would be suggested. Since the $S_e (=65\%)$ of the existing RAS was larger than 40%, the existing RAS was assessed as severe and stenting therapy was suggested, which agrees with the clinical practice for this patient.

4 | SUMMARY AND DISCUSSION

We have presented a computational concept to derive a new, noninvasive, and patient-specific hemodynamic index for assessing the severity of RAS and predicting possible benefits to the patient after the RAS is stented. A developed and validated in-house computational platform of ICH, *InVascular*, is used to quantify the 4-D hemodynamics field in the stenosed arterial systems segmented from patient's CTA imaging data. For an existing stenosis with VR S_e , a hemodynamic relation between TPI and S is established through a parametric deterioration of the volume reduction varying from 0% to 95% with an increment of 5%. Two thresholds, that is, S_m (mild) and S_s (severe), can be derived through two regional slopes on the TPI– S curve. Comparing S_e with S_m and/or S_s , we can assess the hemodynamic severity of the RAS, either mild, severe, or moderate. Such an assessment provides the potential to recommend if the RAS needs to be stented immediately. For a severe RAS, the TPI– S relation also provides a baseline prediction of the TPI improvement from a potential stenting therapy. Six patient cases with 6 aortic and 12 renal arteries are studied. The accuracy of *InVascular* for pressure is demonstrated via an agreement between computed and measured pressure waveforms. The computed and measured systolic pressure values have no statistical difference. UQ shows the 95% confidence interval for each computed systolic pressure. We found that VR, instead of DR, is more sensitive to TSPG, implying that VR is a better indicator of the hemodynamic degree of stenosis. This observation agrees with a previous study in open data and our ongoing study on aortoiliac arterial systems. We applied the computational concept in one study case to derive the hemodynamic index. The existing RAS is assessed as severe, recommending a stenting therapy. This assessment is consistent with the clinical practice for this patient. One of the most attractive advantages of *InVascular* is its fast computation speed utilizing GPU parallel computing, thus it is promising to establish the TPI– S curve within the clinical permitted time, for example, half an hour, as opposed to typical time frames of days or even weeks.

TABLE 4 The study was on the left renal artery of Case VI

Varying VR from 38% to 60% for an RAS with fixed DR (75%)				Varying DR from 53% to 69% for an RAS with fixed VR (45%)			
DR (%)	VR (%)	TSPG (mmHg)	Geometry	VR (%)	DR (%)	TSPG (mmHg)	Geometry
75	38	46		45	53	44	
	50	62			60	50	
	60	84			69	50	

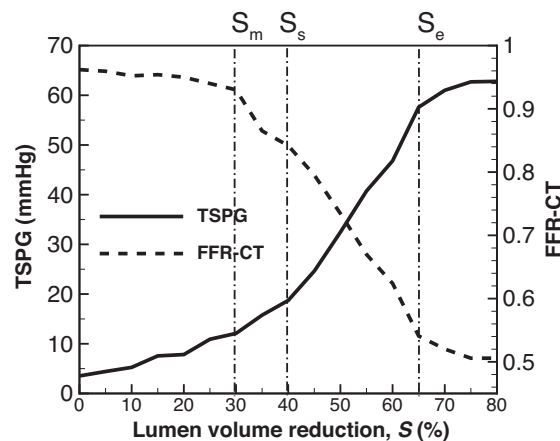


FIGURE 9 Hemodynamic index to assess the severity of the existing RAS in Case VI with VR = 65%. Correlation of mean TSPG (left, solid line) and FFR-CT(right, dashed line) versus volumetric stenosis degree S

The computational concept presented in this work is introductory. We focus on the development of the modeling and computation platform method. All the results are preliminary. The statistical results are based on small case size. The UQ analysis only considers one uncertainty. The finding that VR is more sensitive to TPI the applicability of assessing the RAS severity via two thresholds of VR on the TPI- S is based on one study case. Although we have shown the agreement with open data for the former and the consistency with a medical practice for the latter, a more rigorous study with a much larger case size is critical to demonstrate the reliability and applicability of this computational concept to address the medical need. There remain critical questions beyond this work. Which is more appropriate to determine the severity of RAS, TSPG, or FFR-CT? Is there a gold standard for RAS? What patient group will be benefited? A clinical trial with thousands of patient cases will be needed to address these questions. Meanwhile, real blood flow is non-Newtonian and real vessels are deformable. There often exist multiple or bilateral stenoses in one patient. Adding more modeling components to mimic the real-world vascular system in *InVascular* will be a continuous effort. However, more modeling components are always tied to more computation costs. It is important to balance the need for accuracy and the computation burden. This study considers uncertainty in boundary conditions. There are other uncertainties as discussed in Section 2.3. Uncertainty in the images is also significant, and the methodology of quantifying its effect is still developing. FOSM used in this study is the most efficient UQ method, and its accuracy can be improved using other UQ methods, such as a sampling method, but with much lower efficiency.

Besides the RAS, the computational concept can be applied to arterial stenosis in other vascular beds such as coronary, carotid, cerebral, mesenteric, aortoiliac, and femoropopliteal vascular beds to assess the hemodynamic

severity of stenosis and to predict the potential benefits of vascular interventions to remove the stenosis. Such a capability, after being approved by a medical trial, will greatly aid in surgical decision-making to plan procedures. Avoiding over or under-utilization of invasive therapy will significantly reduce the risk of surgical complications and medical costs.

ACKNOWLEDGMENTS

This research was supported by National Science Foundation Grant No. CBET1803845 and University Fellowship 2017–2018, IUPUI, The Extreme Science and Engineering Discovery Environment (XSEDE), which is supported by National Science Foundation Grant No. ACI-1548562, The Disease Diagnostics Inventors Challenge a competition founded by the Purdue Institute of Inflammation, Immunology and Infectious Disease (PI4D), Renal Imaging Technology Development Program (RITDP), IUPUI Research Center for Quantitative Renal Imaging.

CONFLICT OF INTEREST

The authors declare that there is no conflict of interest that could be perceived as prejudicing the impartiality of the research reported.

DATA AVAILABILITY STATEMENT

The data that support the findings of this study are available upon request for nonprofit use.

REFERENCES

1. Safian RD, Textor SC. Renal artery stenosis. *N Engl J Med*. 2001;344:431-442.
2. Barajas L. Anatomy of the juxtaglomerular apparatus. *Am J Physiol*. 1979;237(5):F333-F343.
3. Koeppen BM, Stanton BA. Glomerular filtration and renal blood flow. *Renal Physiology*. 5th ed. Elsevier; 2013:27-42.
4. Klein AJ, Jaff MR, Gray BH, et al. SCAI appropriate use criteria for peripheral arterial interventions: an update. *Catheter Cardiovasc Interv*. 2017;90:E90-E110.
5. The ASTRAL Investigators. Revascularization versus medical therapy for renal-artery stenosis. *NEJM*. 2009;361:1953-1962.
6. Bax L, Woittiez AJ, Kouwenberg HJ, et al. Stent placement in patients with atherosclerotic renal artery stenosis and impaired renal function: a randomized trial. *Ann Intern Med*. 2009;150(12):840-848.
7. Cooper CJ, Murphy TP, Cutlip DE, Jamerson K. Stenting and medical therapy for atherosclerotic renal artery stenosis. *N Engl J Med*. 2014;27:257-260.
8. Mohan LV, Bouke V. The Management of Renal Artery Stenosis: An alternative interpretation of ASTRAL and CORAL. *Eur J Vasc Endovasc Surg*. 2015;49:465-473.
9. Prince M, Tafur JD, White CJ. When and how should we revascularize patients with atherosclerotic renal artery stenosis? *J Am Coll Cardiol Interv*. 2019;12(6):505-517.
10. Olin JW, Piedmonte MR, Young JR, De Anna S, Grubb M, Childs MB. The utility of duplex ultrasound scanning of the renal arteries for diagnosing significant renal artery stenosis. *Ann Intern Med*. 1995;122:833-836.
11. Pijls NH, De Bruyne B, Peels K, et al. Measurement of fractional flow reserve to assess the functional severity of coronary-artery stenoses. *N Engl J Med*. 1996;334(26):1703-1708.
12. Koo B-K. The present and future of fractional flow reserve. *Circ J*. 2014;78(5):1048-1054.
13. Ridout SJ, Parker BA, Smithmyer SL, Gonzales JU, Beck KC, Proctor DN. Age and sex influence the balance between maximal cardiac output and peripheral vascular reserve. *J Appl Physiol*. 2009;108(3):483-489.
14. Mitchell JA, Subramanian R, White CJ, et al. Predicting blood pressure improvement in hypertensive patients after renal artery stent placement: renal fractional flow reserve. *Catheter Cardiovasc Interv*. 2007;69(5):685-689.
15. Beregi J-P, Mounier-Vehier C, Devos P, et al. Doppler flow wire evaluation of renal blood flow reserve in hypertensive patients with normal renal arteries. *Cardiovasc Intervent Radiol*. 2000;23(5):340-346.
16. Manoharan G, Pijls NHJ, Lameire N, et al. Assessment of renal flow and flow reserve in humans. *J Am Coll Cardiol*. 2006;47(3):620-625.
17. Subramanian R, White CJ, Rosenfield K, et al. Renal fractional flow reserve: a hemodynamic evaluation of moderate renal artery stenoses. *Catheter Cardiovasc Interv*. 2005;64(4):480-486.
18. Kądziela J, Januszewicz A, Prejbisz A, et al. Prognostic value of renal fractional flow reserve in blood pressure response after renal artery stenting (PREFER study). *Cardiol J*. 2013;20(4):418-422.
19. Frauchiger B, Zierler R, Bergelin R, Isaacson J, Strandness D Jr. Prognostic significance of intrarenal resistance indices in patients with renal artery interventions: a preliminary duplex sonographic study. *Cardiovasc Surg*. 1996;4(3):324-330.
20. Mangiacapra F, Trana C, Sarno G, et al. Translesional pressure gradients to predict blood pressure response after renal artery stenting in patients with renovascular hypertension. *Circ Cardiovasc Interv*. 2010;3:537-542.
21. Sawchuk AP, Khan M, Deb A, et al. Noninvasive and patient-specific assessment of true severity of renal artery stenosis for new guidelines for planning stent therapy. *J Vasc Surg*. 2018;68(3):e64-e65.

22. Rundback J, Sacks D, Kent KC, et al. AHA councils on cardiovascular radiology, high blood pressure research, kidney in cardiovascular disease, cardio-thoracic and vascular surgery, and clinical cardiology, and the Society of Interventional Radiology FDA device forum committee. American Heart Association. Guidelines for the reporting of renal artery revascularization in clinical trials. *Circulation*. 2002;106(12):1572-1585.
23. Yu H, Deb A, Khan M, Chen R, Yang Y, Wang I-W. Non-invasive, patient-specific assessment of LVAD modeled with consideration of LV ejection and function. *Circ Res*. 2018;123(Suppl_1):A229.
24. Marsden AL, Esmaily-Moghadam M. Multiscale modeling of cardiovascular flows for clinical decision support. *Appl Mech Rev*. 2015;67:030804.
25. Les AS, Shadden SC, Figueroa CA, et al. Quantification of hemodynamics in abdominal aortic aneurysms during rest and exercise using magnetic resonance imaging and computational fluid dynamics. *Ann Biomed Eng*. 2010;38(4):1288-1313.
26. Antiga L, Piccinelli M, Botti L, Ene-Iordache B, Remuzzi A, Steinman AD. An image-based modeling framework for patient-specific computational hemodynamics. *Med Biol Eng Comput*. 2008;46:1097-1112.
27. Yu H., Zhao Y., Lin C., Unified computational method and system for in vivo patient-specific hemodynamics, US patent 10482215B2, 2019. <https://www.google.com.na/patents/WO2016065161A1?cl=en#backward-citations>
28. Tesche C, De Cecco CN, Albrecht MH, et al. Coronary CT angiography-derived fractional flow reserve. *Radiology*. 2017;285(1):17-33.
29. Zhong L, Zhang J-M, Su B, San Tan R, Allen JC, Kassab GS. Application of patient-specific computational fluid dynamics in coronary and intra-cardiac flow simulations: challenges and opportunities. *Front Physiol*. 2018;9:742.
30. VanGeet O. *Best practices guide for energy-efficient data center design*. EERE Publication and Product Library; 2010.
31. Liu M, Liu G. Smoothed particle hydrodynamics (SPH): an overview and recent developments. *Arch Comput Methods Eng*. 2010;17(1):25-76.
32. Yu HW, Khan M, Sawchuk A, et al. Fast, non-invasive, and patient-specific assessment for ischemic severity of arterial stenosis. *Arterioscler Thromb Vasc Biol*. 2019;39(Suppl_1):A364.
33. Khan M. M. I., Image based computational hemodynamics for non-invasive and patient-specific assessment of arterial stenosis, MS Thesis, Purdue University Graduate School, USA. 2019.
34. Yu H, Chen X, Wang Z, et al. Mass-conserved volumetric lattice Boltzmann method for complex flows with willfully moving boundaries. *Phys Rev E*. 2014;89(6):063304.
35. Wang Z, Yan Z, Qian Y, Chen G. Lattice Boltzmann model of anisotropic diffusion for image denoising, in: information computing and telecommunications (YC-ICT). *2010 IEEE Youth Conference*. IEEE; 2010:21-24.
36. An S, Yu H, Yao J. GPU-accelerated volumetric lattice Boltzmann method for porous media flow. *J Petro Sci Eng*. 2017;156:546-552.
37. An S, Yu H, Wang Z, Chen R, Kapadia B, Yao J. Unified mesoscopic modeling and GPU-accelerated computational method for image-based pore-scale porous media flows. *Int J Heat Mass Trans*. 2017;115:1192-1202.
38. Wang Z, Zhao Y, Sawchuck AP, Dalsing MC, Yu HW. GPU acceleration of volumetric lattice Boltzmann method for patient-specific computational hemodynamics. *Comput Fluids*. 2015;115:192-200.
39. Zhang X, Gomez-Paz J, McDonough J, Islam MM, Andreopoulos Y, Yu H. Volumetric lattice Boltzmann method for wall stresses of image-based pulsatile flows. *Sci Rep*. 2022;12:1697.
40. Yu H, Khan M, Wu H, et al. Inlet and outlet boundary conditions and uncertainty quantification in volumetric lattice Boltzmann method for image-based computational hemodynamics. *Fluids*. 2022;7:30.
41. Kung EO, Taylor CA. Development of a physical Windkessel module to re-create in vivo vascular flow impedance for in vitro experiments. *Cardiovasc Eng Technol*. 2011;2(1):2-14.
42. Khan M, Sawchuk AP, Deb A, et al. Effective three-element Windkessel model based on Doppler ultrasound images for noninvasive quantification of trans-stenotic pressure gradient in aortorenal system. *Circ Res*. 2018;123(Suppl_1):A360.
43. Zhao-Li G, Chu-Guang Z, Bao-Chang S. Non-equilibrium extrapolation method for velocity and pressure boundary conditions in the lattice Boltzmann method. *Chin Phys*. 2002;11(4):366-374.
44. Yu H, Chen R, Wang H, et al. GPU accelerated lattice Boltzmann simulation for rotational turbulence. *Comput Math Appl*. 2014;67(2):445-451.
45. Tran JS, Schiavazzi DE, Kahn AM, Marsden AL. Uncertainty quantification of simulated biomechanical stimuli in coronary artery bypass grafts. *Comput Methods Appl Mech Eng*. 2019;345:402-428.
46. Seo J, Schiavazzi D, Marsden A. Uncertainty quantification for patient-specific cardiovascular simulations in high-performance computing. *Bulletin of the American Physical Society*, 2018 Nov 20;63.
47. Wu H, Khan M, Du X, Sawchuk AP, Yu HW. Reliability analysis for image-based non-invasive pressure quantification in Aortorenal artery systems. *Circ Res*. 2019;125(Suppl_1):A122.
48. Zang TA. *Needs and Opportunities for Uncertainty-Based Multidisciplinary Design Methods for Aerospace Vehicles*. National Aeronautics and Space Administration, Langley Research Center; 2002.
49. Roy CJ, Oberkampf WL. A comprehensive framework for verification, validation, and uncertainty quantification in scientific computing. *Comput Methods Appl Mech Eng*. 2011;200(25-28):2131-2144.
50. Cruse T, Brown J. Transitioning NDA form research to engineering design. In: Nilolaidis E, Chiocel DM, Singhal S, eds. *Engineering Design Reliability Handbook*. CRC Press; 2005.
51. Zhu Z, Du X. Reliability analysis with Monte Carlo simulation and dependent kriging predictions. *J Mech Des*. 2016;138(12):121403-1-11.
52. Wang Z, Wang P. A new approach for reliability analysis with time-variant performance characteristics. *Reliab Eng Syst Safety*. 2013;115:70-81.

53. Wang Z, Chen W. Confidence-based adaptive extreme response surface for time-variant reliability analysis under random excitation. *Struct Safety*. 2017;64:76-86.
54. Zhuang X, Pan R, Du X. Enhancing product robustness in reliability-based design optimization. *Reliab Eng Syst Safety*. 2015;138:145-153.
55. Wei X, Du X. Robustness metric for robust design optimization under time-and space-dependent uncertainty through metamodeling. *J Mech Des*. 2020;142(3):031110-1-10.
56. Du X. Toward time-dependent robustness metrics. *J Mech Des*. 2012;134(1):011004-1-8.
57. Rockafellar RT. Coherent approaches to risk in optimization under uncertainty. *OR Tools and Applications: Glimpses of Future Technologies*. Informa; 2007:38-61.
58. Beck AT, de Santana Gomes WJ. A comparison of deterministic, reliability-based and risk-based structural optimization under uncertainty. *Probabil Eng Mech*. 2012;28:18-29.
59. Lee TW, Kwak BM. A reliability-based optimal design using advanced first order second moment method. *J Struct Mech*. 1987;15(4):523-542.
60. Huang B, Du X. Probabilistic uncertainty analysis by mean-value first order saddlepoint approximation. *Reliab Eng Syst Safety*. 2008;93(2):325-336.
61. Du X, Sudjianto A. First order saddlepoint approximation for reliability analysis. *AIAA J*. 2004;42(6):1199-1207.
62. Caruso MV, De Rosa S, Indolfi C, Fragomeni G. Computational analysis of stenosis geometry effects on right coronary hemodynamics. *2015 37th Annual International Conference of the IEEE Engineering in Medicine and Biology Society (EMBC)*. IEEE; 2015:981-984.

How to cite this article: Yu H, Khan M, Wu H, et al. A new noninvasive and patient-specific hemodynamic index for the severity of renal stenosis and outcome of interventional treatment. *Int J Numer Meth Biomed Engng*. 2022;38(7):e3611. doi:[10.1002/cnm.3611](https://doi.org/10.1002/cnm.3611)